



Publication Year	2020
Acceptance in OA @INAF	2021-11-23T11:44:24Z
Title	The eye of Gaia on globular clusters structure: tidal tails
Authors	SOLLIMA, ANTONIO LUIGI
DOI	10.1093/mnras/staa1209
Handle	http://hdl.handle.net/20.500.12386/31125
Journal	MONTHLY NOTICES OF THE ROYAL ASTRONOMICAL SOCIETY
Number	495

The eye of *Gaia* on globular clusters structure: tidal tails

A. Sollima  

INAF – Osservatorio di Astrofisica e Scienza dello spazio di Bologna, via Gobetti 93/3, I-40129 Bologna, Italy

Accepted 2020 April 25. Received 2020 April 22; in original form 2020 January 23

ABSTRACT

I analyse the projected density distribution of member stars over a wide area surrounding 18 Galactic globular clusters using the photometric and astrometric information provided by the second data release of the *Gaia* mission. A 5D mixture modelling technique has been employed to optimally isolate the signal of the cluster stellar population from the contamination of the Galactic field, taking advantage of its different distribution in the space formed by colours, magnitudes, parallaxes, and proper motions. In 7 clusters I detect collimated overdensities at a $>3\sigma$ level above the background density extending well beyond the cluster tidal radius, consistent with the distortion expected as a result of the tidal interaction with the Milky Way potential. In five of these clusters (NGC 288, NGC 2298, NGC 5139, NGC 6341, and NGC 7099) spectacular tidal tails extend up to the border of the analysed field of view at 5 deg from the centre. At large distances from the cluster centre, the orientation of the detected overdensities appears to be systematically aligned with the cluster orbital path, in agreement with the predictions of N -body simulations. The fraction of stars contained in the tidal tails of these clusters is also used to determine the first observational estimate of their present-day destruction rates.

Key words: methods: statistical – stars: kinematics and dynamics – stars: Population II – globular clusters: general.

1 INTRODUCTION

Any stellar system immersed in a gravitational potential is subject to its tidal strain. In particular, the presence of the external potential introduces a repulsive centrifugal term that adds to the internal gravitational potential and determines an anisotropic shape of the effective potential contours. The effect of tidal distortion is more pronounced at large distances from the centre where tidal forces dominate over the internal gravitation. Globally, the zero-velocity surfaces have a characteristic elongated shape (Roche lobe) with two saddle points (the so-called ‘Lagrangian points’, located at a distance from the cluster centre called ‘Jacobi radius’) and aligned with the direction of the galactic potential gradient (i.e. towards the Galactic Centre; Binney & Tremaine 1987). Stellar orbits confined in the outer region of the stellar system are therefore distorted towards the Lagrangian points and the stellar density follows the shape of the Roche lobe. A star with orbital energy exceeding the effective potential at the Lagrangian points can escape from the system if its orbit crosses an aperture around these points, whose size depends on its energy excess (Fukushige & Heggie 2000). Once escaped, the star initially moves away from the satellite following the path along its escape direction i.e. radially along the satellite-galactic centre direction. As the distance of the star increases, the Coriolis force becomes significant pushing the star towards the

same orbital path of its original stellar system. The appearance of the whole system is therefore characterized by the presence of a pair of symmetric tails emerging from the satellite and following a S-shape (Montuori et al. 2007; Klimentowski et al. 2009). The stars in the tidal tails become independent satellites with integrals of motion similar to those of their original host stellar system, and therefore follow its orbit with a slightly different orbital period. Stars escaped at early epochs accumulate a large phase delay and are therefore more distant from the satellite than those recently escaped. So, the orientation and prominence of tidal tails provide crucial information on the orbit and the recent mass-loss history of a stellar system.

Examples of tidal features have been observed in interacting galaxies (Duc et al. 2015) and around the most recent accretion events occurred in the Milky Way and M31 (Ibata, Gilmore & Irwin 1994; Ibata et al. 2001). All these systems are characterized by large mass-loss rates (up to 10^8 stars Gyr^{-1} ; Fardal et al. 2006; Law & Majewski 2010) leaving observational features easily detectable with imaging techniques as surface brightness or star counts excess (Belokurov et al. 2006a; Martínez-Delgado et al. 2010).

The detection of tidal tails is more challenging in star clusters, characterized by a significantly smaller mass-loss rate ($\sim 10^{2-4}$ star Gyr^{-1} ; Dinescu, Girard & van Altena 1999). The stars in the tails constitute indeed a tiny fraction (< 0.1 per cent) of those contained in the region surrounding the cluster, mainly populated by Galactic interlopers. For this reason, filtering techniques are used to maximize the signal of the cluster by assigning weights to stars according to their position in the colour–magnitude diagram (the

* E-mail: antonio.sollima@inaf.it

‘matched-filter’; Rockosi et al. 2002). Thanks to this technique, it has been possible to detect tidal features around many globular clusters (GCs; Grillmair et al. 1995; Leon, Meylan & Combes 2000; Chun et al. 2010, 2015; Chen & Chen 2010; Jordi & Grebel 2010; Carballo-Bello et al. 2018; Shipp et al. 2018) and open clusters (Bergond, Leon & Guibert 2001; Dalessandro et al. 2015). Most of these studies discovered only deformations of the density contours close to the clusters’ tidal radii interpreted as the result of tidal effects. Spectacular exceptions are constituted by the 30°-long tail detected around Palomar 5 (Odenkirchen et al. 2001; Erkal, Koposov & Belokurov 2017) and, to a less extent, the tidal tails detected in NGC 5466 (Belokurov et al. 2006b), Palomar 1, (Niederste-Ostholt et al. 2010), Palomar 14 (Sollima et al. 2011), Eridanus and Palomar 15 (Myeong et al. 2017), and NGC 7492 (Navarrete, Belokurov & Koposov 2017).

The second data release of the *Gaia* mission (Gaia Collaboration 2018a) recently provided (beside colours and magnitudes) parallaxes and proper motions for $\sim 1.3 \times 10^9$ stars across the entire sky, allowing to increase the number of dimensions of the parameter space where to select cluster members. Thanks to this data set it has been possible to detect extended tidal tails in NGC 5139 (Ibata et al. 2019a), NGC 288 (Kaderali et al. 2019), NGC 362 (Carballo-Bello 2019), NGC 3201 (Bianchini, Ibata & Famaey 2019), NGC 5904 (Grillmair 2019), and around a few open clusters (Tang et al. 2019; Röser, Schilbach & Goldman 2019; Röser & Schilbach 2019).

In this paper, I perform a systematic search for tidal tails around a sample of 18 nearby GCs using the full 5D parameter space provided by *Gaia* data. In Section 2, the analysed sample of GCs, together with the description of the adopted data set is presented. The algorithm adopted to determine the projected density map is described in Section 3 and the results of the analysis are presented in Section 4. Finally, the conclusions are presented in Section 5.

2 OBSERVATIONAL MATERIAL

2.1 GC sample

The GCs analysed in this paper have been selected as those with the largest probability of detection of low-surface brightness features. Many factors affect this probability, among them: (i) the amount of mass lost in recent epochs, (ii) the fraction of the cluster stellar population sampled by the adopted catalogue, (iii) the density of Galactic field stars, and (iv) the separation of cluster and field stars in the considered parameter space.

Although theoretical predictions of the mass-loss rate of GCs exist in the literature (Gnedin & Ostriker 1997; Allen, Moreno & Pichardo 2006), many uncertainties affect these estimates (due to the uncertainties in the adopted Galactic potential, GC space velocities, recipes for mass-loss, etc.). So no selection has been made on the basis of this parameter. On the other hand, even in case of large mass-loss rates, the tidal tails of low mass, and/or distant GCs will be sampled only with a small number of stars. For this reason, I excluded GCs with integrated apparent magnitude $V > 9.5$.

The fraction of sampled cluster stellar population depends mainly on the fraction of main-sequence stars brighter than the limiting magnitude of *Gaia* and therefore on the cluster heliocentric distance. The GCs analysed here were selected among those at distances $d_{\odot} < 15$ kpc (from Harris 1996, 2010 edition). Considering the *Gaia* limiting magnitude ($20 < G_{\text{cut}} < 21$; see Section 2.2), this corresponds to ~ 1 mag below the turn-off of a typical old and metal-poor ($t > 10$ Gyr; $[\text{Fe}/\text{H}] < -1$) GC stellar population (Bressan et al. 2012).

Table 1. GCs analysed in this work (column 1). The detection of significant tidal tails, according to the criteria described in Section 4.1 is reported in column (2) and the destruction rate, where available, is listed in column (3).

NGC	Tidal tails	ν Gyr $^{-1}$
288	Y	0.033 ± 0.003
1851	N	
1904	N	
2298	Y	0.057 ± 0.007
2808	N	
3201	N	
4590	N	
5139	Y	0.019 ± 0.002
5272	N	
5897	N	
5904	Y	
6205	N	
6341	Y	0.018 ± 0.001
6362	Y	
6752	N	
7078	N	
7089	N	
7099	Y	0.085 ± 0.004

To limit the fraction of Galactic disc and bulge interlopers, I excluded those GCs lying at latitudes $|b| < 10^\circ$ and at a projected distance from the Galactic Centre $R_{\text{GC}} < 30^\circ$. I also excluded NGC 104 and NGC 362 because of the contamination from Small Magellanic Cloud stars in the background of these clusters.

Some nearby GCs, in spite of their projected position in the sky, have a mean proper motions significantly different from that of the surrounding Galactic population. The stellar population of these GCs can be easily isolated allowing an efficient analysis. Among these GCs I included in the sample NGC 3201 (with a systemic proper motion different by $\Delta\mu \sim 14$ mas yr $^{-1}$ from the mean proper motion of the field population), in spite of its low latitude ($b = 8^\circ 64'$).

Instead, the GC NGC 5286 has been excluded because of the extremely high small-scale spatial variation of the *Gaia* catalogue completeness even at bright magnitudes ($G_{\text{cut}} < 20$; see Section 2.2).

The final sample consists of 18 GCs (see Table 1), ~ 12 per cent of the entire Milky Way GC system, and constitutes one of the most extensive sample adopted for this kind of studies.

2.2 *Gaia* catalogue selection

The analysis performed here is entirely based on data provided by the *Gaia* second data release (Gaia Collaboration 2018a). This survey measured parallaxes, proper motions, magnitudes, and colours for 1.3×10^9 stars in the entire sky, including almost all known Galactic GCs in both hemispheres. The catalogue has a formal limiting magnitude of $G = 21$, although this value depends on celestial position. Moreover, the source completeness varies with a patchy structure characterized by source density fluctuations that reflect the scan law pattern of the survey (Arenou et al. 2018).

For each GC, the full set of information of all sources contained in a circle with radius of 5° centred on the GC centre has been retrieved. It consists of G magnitudes, $G_{\text{BP}} - G_{\text{RP}}$ colours, parallaxes (p), proper motions (μ_{α}^* , μ_{δ}) together with their associated uncertainties and corresponding covariances. Uncertainties in parallaxes have been corrected using the prescriptions of Lindegren et al. (2018). The G magnitudes and $G_{\text{BP}} - G_{\text{RP}}$ colours have been corrected

for interstellar extinction using the reddening maps of Lallement et al. (2019)¹ and the extinction coefficients by Casagrande & VandenBerg (2018).

To maximize the detection efficiency avoiding to introduce any bias, no selection has been made on the basis of the *Gaia* quality flags. It has indeed been shown that the second *Gaia* data release is characterized by spatial variation of the astrometric accuracy occurring at both small and large scales (from a few arcmin to several degrees) with a patchy distribution across the sky, depending on the local stellar density, and the satellite scanning law (Arenou et al. 2018). So, any cut made on the basis of astrometric quality parameters would spuriously decrease the stellar density of the less surveyed regions. On the other hand, the inclusion of stars with poorly measured astrometric/photometric parameters increases the noise in the density determination, so that the cost-effectiveness of the application of quality cuts is not trivial to be assessed. As a test, I compared the density maps of the GC NGC 5139, where tidal tails were already detected using the same data set adopted here (Ibata et al. 2019a), derived with and without the application of various cuts in parallax/proper motion errors: the inclusion of quality cuts, while requiring a fine tuning to avoid the emergence of patches parallel to the *Gaia* scanning law, produces no significant improvement in the detection of tidal tails. So, the only selection applied to the catalogue has been made on the basis of the deredded *G* magnitude. Indeed, for the reliability of this analysis, it is crucial to ensure a constant source detection efficiency across the analysed field of view, and the completeness fluctuations of *Gaia* at its faint end can significantly affect the results of the analysis. The adopted magnitude cut (G_{cut}) varies from cluster to cluster and has been set to ensure a smooth variation of the density across the analysed field of view. For this purpose, the following procedure has been adopted:

- (i) For different guesses of G_{cut} , the sources with $|G - G_{\text{cut}}| < 0.25$ have been selected;
- (ii) The field of view has been divided in 6 arcmin \times 6 arcsec bins evenly distributed within an annulus with internal and external radii of 1° and 5° around the cluster centre, and the number of selected sources contained in each bin has been counted;
- (iii) The logarithm of star counts has been fitted by a first-order polynomial in $(X, Y, \log N)$ and the rms of the fit has been calculated;
- (iv) The largest value of G_{cut} ensuring a rms < 0.05 dex has been adopted.

The values of G_{cut} determined according to the above procedure lie in the range $20 < G_{\text{cut}} < 21$, with brighter cuts in those GCs located in densely populated regions (i.e. close to the Galactic plane and/or the bulge) or characterized by a small number of *Gaia* passages.

Corrected distances (X, Y) and proper motions have been calculated using an orthographic projection of the canonical celestial coordinates and proper motions (see equation 2 of Gaia Collaboration 2018b).

3 METHOD

The algorithm adopted in this work is a 5D mixture modelling (McLachlan & Basford 1988). Schematically, the distribution of a representative sample of cluster members and Galactic field

¹Although the reddening maps of Lallement et al. (2019) are calculated using only stars up to 3 kpc from the Sun, at Galactic latitudes $|b| > 10^\circ$ they include more than 99.9 per cent of the dust column density along the line of sight of all the GCs analysed in this work.

stars in the parameter space is modelled with suitable analytic functions. The relative normalization of the model cluster and field distributions is calculated through a maximum-likelihood technique using samples of stars located in different region of the analysed field and used to determine the local density of cluster stars.

The stars contained within (outside) $\Delta R < 0.5^\circ$ from the cluster centre (from Goldsbury, Heyl & Richer 2013), $\Delta\mu < 2 \text{ mas yr}^{-1}$ from the systemic cluster motion (from Baumgardt et al. 2019)², and $\Delta p < 5\epsilon_p$ from the measured cluster parallax (from Gaia Collaboration 2018b; where ϵ_p is the parallax error) have been selected as *reference samples* for the cluster (field) population.

The parallax distribution of cluster stars has been assumed to be a Dirac delta centred on the mean cluster parallax. This is a reasonable assumption since the parallax differences among cluster stars are more than 100 times smaller than the typical parallax uncertainty in all the GCs of the sample. So, the probability ($P_{p,i}^c$) for a star to be a cluster member, on the basis of its parallax only, is given by

$$\ln P_{p,i}^c = -\frac{(p_i - \langle p \rangle_c)^2}{2\epsilon_{p,i}^2} - \ln(\epsilon_{p,i}), \quad (1)$$

where p_i and $\epsilon_{p,i}$ are the parallax of the i -th star and its associated uncertainty and $\langle p \rangle_c$ is the mean cluster parallax in units of *mas*. The distribution of field star parallaxes has been fitted with the empirical function

$$\Gamma(p) = \left(1 + \frac{p}{a_1}\right)^{-\alpha_1} \left(1 + \frac{p}{a_2}\right)^{-\alpha_2}. \quad (2)$$

The best-fitting values of $a_1, a_2, \alpha_1,$ and α_2 have been determined using a Monte Carlo scheme. For any guess of the $a_1, a_2, \alpha_1,$ and α_2 parameters, N_f (equal to the number of *reference sample* field stars) synthetic parallaxes have been randomly extracted from the corresponding $\Gamma(p)$ distribution (equation 2). Real and synthetic star parallaxes have been sorted and a Gaussian shift with dispersion equal to the parallax uncertainty of each star has been added to the corresponding particle. The cumulative distributions of real and synthetic parallaxes have been then compared using a Kolmogorov–Smirnov test and the values of the parameters providing the largest KS probability have been chosen. The probability for a star to be a field star, on the basis of its parallax, is given by

$$\ln P_{p,i}^f = \ln \int_0^{+\infty} \Gamma(p) \exp\left[-\frac{(p - p_i)^2}{2\epsilon_{p,i}^2}\right] dp - \ln\left(\sqrt{2\pi}\epsilon_{p,i} \int_0^{+\infty} \Gamma(p) dp\right). \quad (3)$$

The distribution of cluster stars in the proper motions space has been modelled with a 2D Gaussian with a decreasing dispersion as a function of distance from the cluster centre according to the prediction of the King (1966) model best fit of de Boer et al. (2019). The normalization of the model proper motion dispersion profile has been chosen by maximizing the log-likelihood

$$\begin{aligned} \ln L &= \sum_{i=1}^N \ln P_{\mu,i} \\ \ln P_{\mu,i} &= -\frac{1}{2} [\delta X_i^2 + \delta Y_i^2 - 2\tilde{\rho}_i \delta X_i \delta Y_i + \ln(1 - \tilde{\rho}_i^2) \\ &\quad + \ln(s_{\mu X,i}^2 s_{\mu Y,i}^2)] - \ln(2\pi) \end{aligned} \quad (4)$$

²For NGC 5139, because of its large extent and velocity dispersion, these conditions have been set to $\Delta R < 0.8^\circ$ and $\Delta\mu < 2.3 \text{ mas yr}^{-1}$.

where

$$\begin{aligned}\delta X_i^2 &= \frac{(\mu_{\alpha,i}^* - \langle \mu_{\alpha}^* \rangle_c)^2}{(1 - \tilde{\rho}_i^2) s_{\mu X,i}^2} \\ \delta Y_i^2 &= \frac{(\mu_{\delta,i} - \langle \mu_{\delta} \rangle_c)^2}{(1 - \tilde{\rho}_i^2) s_{\mu Y,i}^2} \\ s_{\mu X,i}^2 &= \epsilon_{\mu\alpha,i}^2 + \sigma^2(R_i) \\ s_{\mu Y,i}^2 &= \epsilon_{\mu\delta,i}^2 + \sigma^2(R_i) \\ \tilde{\rho}_i &= \frac{\rho_i \epsilon_{\mu\alpha,i} \epsilon_{\mu\delta,i}}{s_{\mu X,i} s_{\mu Y,i}}\end{aligned}\quad (5)$$

among the $N = N_c$ *reference sample* cluster stars. In the above equations, $\langle \mu_{\alpha}^* \rangle_c$ and $\langle \mu_{\delta} \rangle_c$ are the systemic cluster proper motions, $\mu_{\alpha,i}^*$ and $\mu_{\delta,i}$ are the proper motions of the i -th star, $\epsilon_{\mu\alpha,i}$, $\epsilon_{\mu\delta,i}$ are the proper motion errors, ρ_i is the correlation coefficient of the two uncertainties and $\sigma(R_i)$ is the normalized model proper motion dispersion at the projected distance of the i -th star (in units of mas yr^{-1}). For the field population, the proper motion distribution has been modelled with a 2D tilted Gaussian function with parallax-dependent dispersion

$$\sigma(p) = \frac{a}{p} \{1 + \exp[b(\log p - c)]\}.\quad (6)$$

The values of the free parameters a , b , c , and θ have been derived by maximizing the log-likelihood of equation (4) applied to the *reference sample* field stars ($N = N_f$) and using

$$\begin{aligned}\delta X_i^2 &= \frac{\left[(\mu_{\alpha,i}^* - \langle \mu_{\alpha}^* \rangle_f) \cos \theta + (\mu_{\delta,i} - \langle \mu_{\delta} \rangle_f) \sin \theta \right]^2}{(1 - \tilde{\rho}_i^2) (s_{X,i}^2 + \sigma^2(p_i))} \\ [5pt] \delta Y_i^2 &= \frac{\left[-(\mu_{\alpha,i}^* - \langle \mu_{\alpha}^* \rangle_f) \sin \theta + (\mu_{\delta,i} - \langle \mu_{\delta} \rangle_f) \cos \theta \right]^2}{(1 - \tilde{\rho}_i^2) (s_{Y,i}^2 + \sigma^2(p_i))} \\ [5pt] s_{X,i}^2 &= \epsilon_{\mu\alpha,i}^2 \cos^2 \theta + \epsilon_{\mu\delta,i}^2 \sin^2 \theta + \rho_i \sin 2\theta \epsilon_{\mu\alpha,i} \epsilon_{\mu\delta,i} \\ [5pt] s_{Y,i}^2 &= \epsilon_{\mu\alpha,i}^2 \sin^2 \theta + \epsilon_{\mu\delta,i}^2 \cos^2 \theta - \rho_i \sin 2\theta \epsilon_{\mu\alpha,i} \epsilon_{\mu\delta,i} \\ [5pt] \tilde{\rho}_i &= \frac{(s_{Y,i}^2 - s_{X,i}^2) \sin 2\theta + 2(\rho_i s_{X,i} s_{Y,i} \cos 2\theta)}{2\sqrt{(s_{X,i}^2 + \sigma^2(p_i)) (s_{Y,i}^2 + \sigma^2(p_i))}},\end{aligned}\quad (7)$$

where $\langle \mu_{\alpha}^* \rangle_f$ and $\langle \mu_{\delta} \rangle_f$ are the mean systemic proper motion of *reference* field stars in the two directions.³

The density of *reference sample* cluster stars at the position of the i -th star in the ($G_{\text{BP}} - G_{\text{RP}}$), G colour–magnitude diagram (Λ_{CMD}) has been calculated using a k -nearest neighbour algorithm (with $k = 10$) and assuming a metric between colours and magnitudes ($\Delta_{G_{\text{BP}}-G_{\text{RP}}}$, Δ_G) = (1, 6) i.e. corresponding to the average ratio of standard deviations in colours and magnitudes of *reference sample*

cluster stars in the considered sample of GCs.

$$\Lambda_{\text{CMD}_i} = \frac{10}{\pi \left[\Delta_{G_{\text{BP}}-G_{\text{RP}}}^2 + \left(\frac{\Delta_G}{6} \right)^2 \right]},$$

where $\Delta_{G_{\text{BP}}-G_{\text{RP}}}$ and Δ_G are the colour and magnitude difference between the i th star and its 10th nearest neighbour. The corresponding cluster membership probability is given by

$$\ln P_{\text{CMD},i}^c = \ln \Lambda_{\text{CMD},i}^c - \ln N_c.\quad (8)$$

The field probability has been calculated using same algorithm applied to the *reference sample* of field stars with $\Delta \log p < 0.1$ from the considered star

$$\ln P_{\text{CMD},i}^f = \ln \Lambda_{\text{CMD},i}^f - \ln N_{f,i},\quad (9)$$

where $N_{f,i}$ is the number of *reference sample* field stars contained in the interval encompassing the parallax of the i -th star.⁴

The total membership probability to the cluster (field) population has been obtained from equations (1), (4), (5), and (8) (and 3, 4, 7, 9, respectively) as

$$\ln P_i^c = \ln P_{p,i}^c + \ln P_{\mu,i}^c + \ln P_{\text{CMD},i}^c$$

$$\ln P_i^f = \ln P_{p,i}^f + \ln P_{\mu,i}^f + \ln P_{\text{CMD},i}^f.$$

Stars with a larger difference $\Delta \ln P \equiv \ln P^c - \ln P^f$ are those lying in a region of the parameter space with a larger contrast between cluster and field distributions (see Fig. 1).

The probabilities of stars located in different regions of the analysed field of view have been then used to derive the relative fraction of cluster-to-field stars. For this purpose, a grid with knots separated by 6 arcmin in both directions has been defined and stars contained within a projected distance R_{lim} from each knot have been selected. In two cases (NGC 5272 and NGC 5904) a nearby GC is present within the field of view (NGC 5466 and Pal 5, respectively). For these cases, the area surrounding the nearby clusters has been masked (see Figs 2 and 3). In each subsample of stars, the cluster-to-field ratio (η) has been chosen as the one maximizing the likelihood

$$\ln L = \sum_{i=1}^{N_{xy}} \eta \ln P_i^c + (1 - \eta) \ln P_i^f$$

and the corresponding density of cluster members is given by

$$\Sigma(X, Y) = \frac{\eta N_{xy}}{A(R_{\text{lim}})},\quad (10)$$

where N_{xy} and $A(R_{\text{lim}})$ are the number of stars in the subsample and its corresponding area.

The choice of R_{lim} should be adaptive to ensure a better resolution in regions with a large number of cluster members and a large smoothing in poorly populated regions. I adopted in each knot of the grid the minimum value of R_{lim} providing $\eta N_{xy} > 100$.

³Note that the simplified functional forms of the parallax (equation 2) and proper motion (equation 6) distribution of field stars were chosen to adequately fit the observed distribution of *reference* field stars without adding a large number of free parameters. This choice is justified by the fact that, while a proper modelling of these distributions would require to account for the projection of the density and velocity ellipsoids of the various Galactic components along the various line of sights, as well as the *Gaia* selection function, the small-scale variations of such distributions are smoothed by the relatively large observational errors.

⁴It should be noted that, at odds with the parallax and proper motion probabilities calculated convolving intrinsic distributions with individual uncertainties, the probability linked to the position in the CMDs includes the global effect of photometric uncertainties neglecting individual differences (i.e. I assigned the same probability to all stars lying in the same portion of the CMD, regardless of their individual colour/magnitude uncertainties). Again, this approximation is made to avoid a complex modelling of the intrinsic distribution in the colour–magnitude–parallax space which depends on many uncertain parameters (like star formation history, mass function, photometric completeness, mass segregation, etc.).

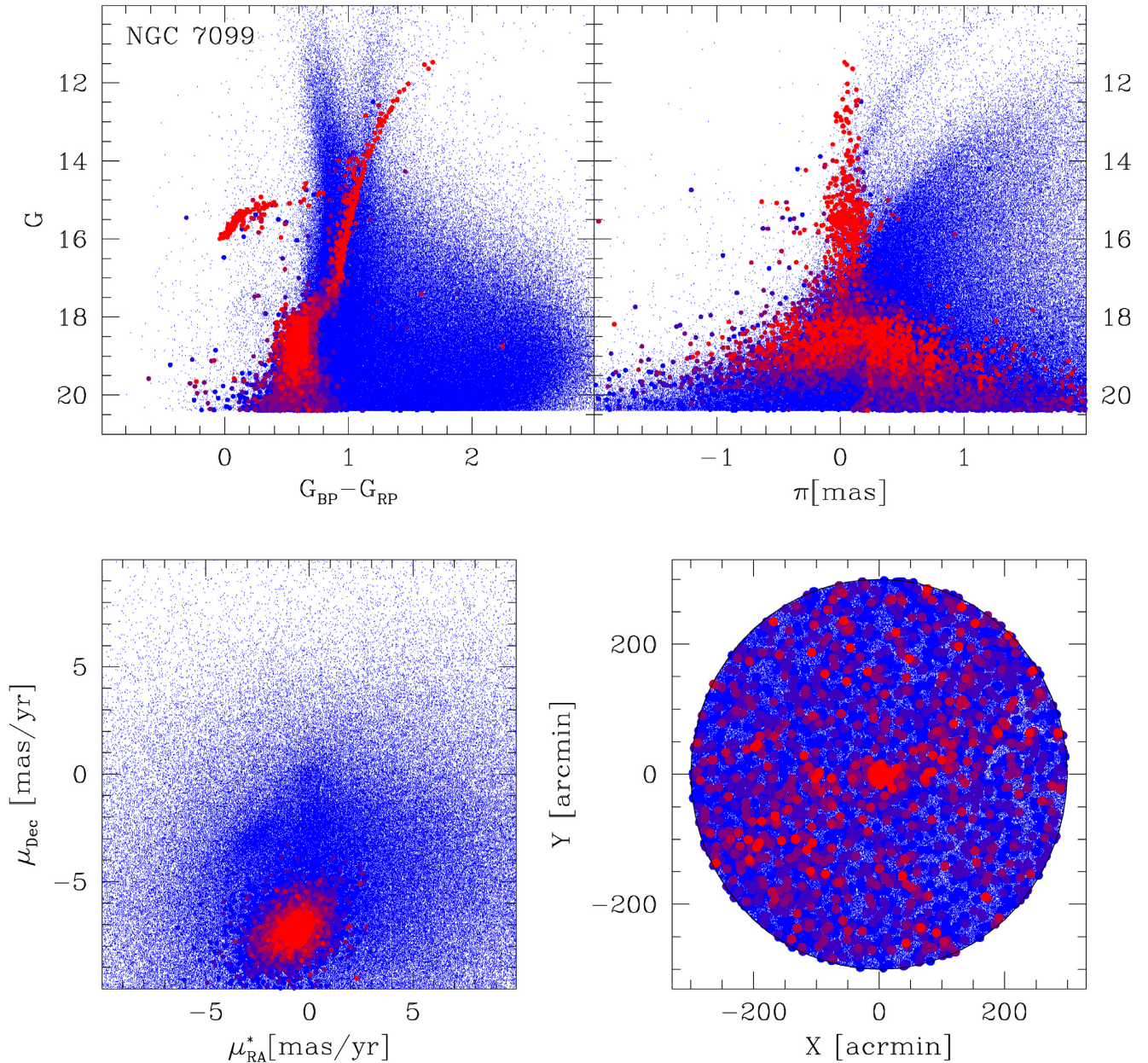


Figure 1. Distribution of NGC 7099 stars in several planes of the parameter space. Top-left: $G_{BP} - G_{RP}$, G colour–magnitude diagram; top-right: parallax– G magnitude plane; Bottom-left: proper motions plane; Bottom-right: projected positions map. Stars with increasing cluster-to-field probability contrast $\Delta \ln P$ are plotted with colours from blue to red (grey to black in the printed version of the paper).

The above procedure should in principle provide a background-subtracted density map. On the other hand, an implicit assumption is that the adopted distribution of field stars in the parameter space does not vary within the field of view. While this is a reasonable assumption in many GCs of the sample, in GCs located in regions characterized by steep variation of the field population properties (i.e. those at low Galactic latitudes and/or close to the bulge) this approximation leads to a gradient in the derived density. However, given the relatively small size of the considered field of view, such a gradient has a small amplitude and varies smoothly across the field of view. For this purpose, the logarithm of the 2D density of regions at distances $R > 2^\circ$ from the cluster centre has been fitted with a first-order polynomial in the $(X, Y, \log \Sigma)$ space and subtracted.

The significance of the derived density has been estimated using a Monte Carlo technique. A sample of 10^3 extractions has been made by randomly reshuffling the position angles of all sources and calculating the corresponding density map. The rms of the various density determinations at distances $R > 2^\circ$ from the cluster centre has been adopted as the typical uncertainty.

4 RESULTS

4.1 Density maps

The projected density maps for the 18 GCs of the sample are shown in Figs 2 and 3. It is apparent that, while the density contours near

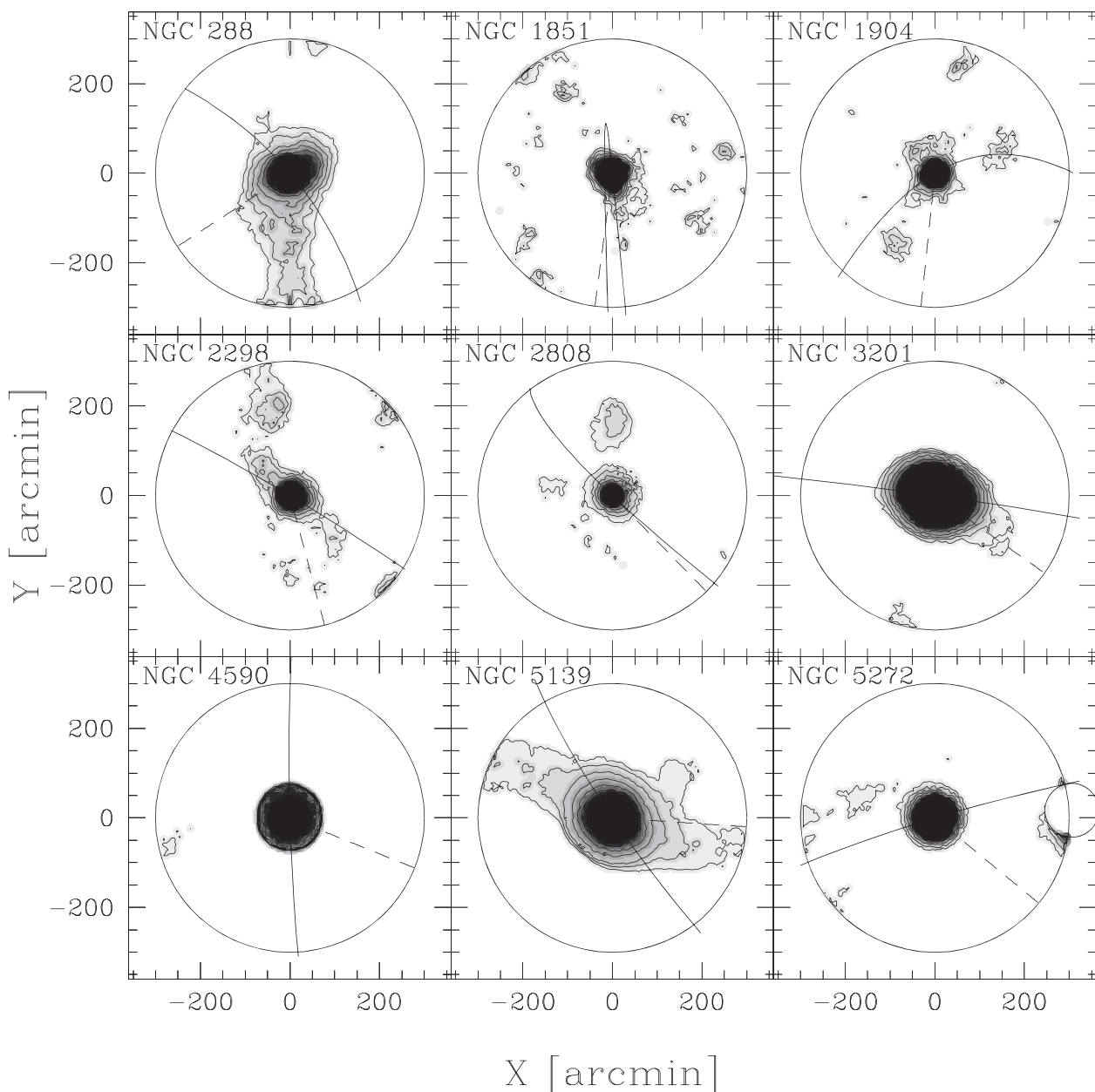


Figure 2. Projected density map for the GCs NGC 288, NGC 1851, NGC 1904, NGC 2298, NGC 2808, NGC 3201, NGC 4590, NGC 5139, and NGC 5272. Contours from 2σ to 10σ above the background density are plotted in logarithmic scale in steps of 1σ . The cluster orbital path and the direction to the Galactic Centre are overlotted as solid and dashed lines, respectively.

the cluster centres are extremely regular, at large distances many clusters show anisotropic density distributions.

None of the previous works on this subject defined a rigorous criterion to claim the detection of tidal tails. Following the definition of tidal tails as ‘a collimated overdensity of stars emerging from the cluster in opposite directions’ (Toomre & Toomre 1972) I defined the two following criteria:

- (i) The closed iso-density contour at 3σ above the background density containing the cluster centre must exceed a distance of 1.5 times the orbit-averaged Jacobi radius;
- (ii) The integrated projected density measured in opposite sectors must be significantly larger than that measured in the complementary region of the sky outside the Jacobi radius.

The first criterion implies the presence of the cluster population outside the Roche lobe. The orbit-averaged Jacobi radius (R_J) has been calculated by averaging over the orbit the Jacobi radius estimated using equation (A2) of Allen et al. (2006) and the GC masses by Baumgardt et al. (2019). The cluster orbit has been integrated within the Galactic potential of Johnston, Spergel & Hernquist (1995) using a fourth-order Runge–Kutta integrator adopting the present-day systemic velocities listed by Baumgardt et al. (2019).

The second criterion requires that the observed overdensity is preferentially oriented in one direction. For this purpose the annulus between R_J and $2R_J$ has been divided in two complementary regions constituted by opposite sectors of 90° width centred at a given position angle (see fig. 5 of Sollima et al. 2011). For each

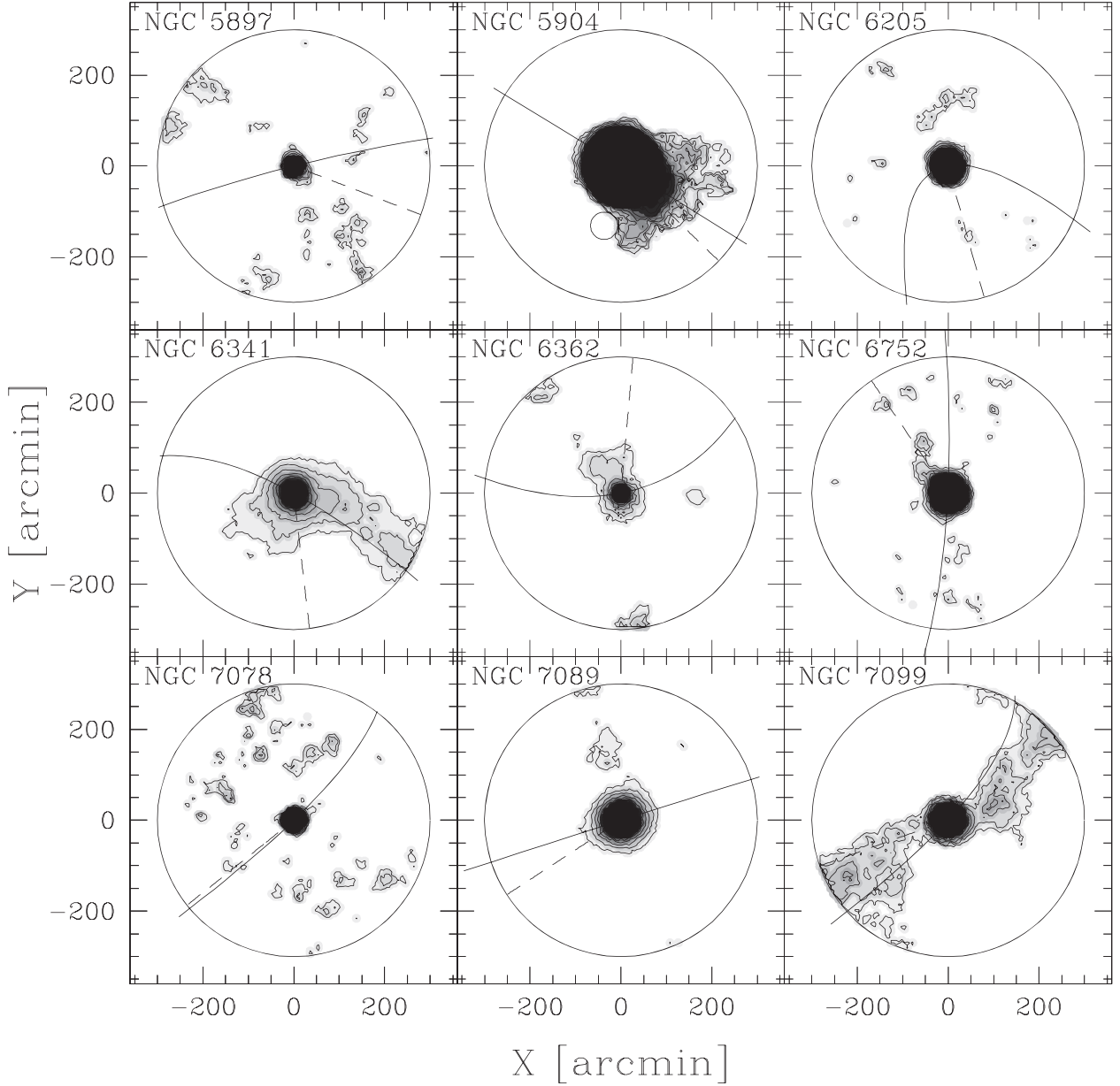


Figure 3. Same as Fig. 2 for NGC 5897, NGC 5904, NGC 6205, NGC 6341, NGC 6362, NGC 6752, NGC 7078, NGC 7089, and NGC 7099.

position angle, the ratio between the densities (measured using equation 10) within each region has been calculated, and the position angle providing the maximum ratio (\mathcal{R}_{\max}) has been chosen. The same estimate has been made in the Monte Carlo randomized extractions (see Section 3) and compared with \mathcal{R}_{\max} . The alignment is considered statistically significant if \mathcal{R}_{\max} is found to be larger than the same value measured in at least 997 (out of 1000) Monte Carlo extractions.

Seven GCs pass the above criteria: NGC 288, NGC 2298, NGC 5139, NGC 5904, NGC 6341, NGC 6362, and NGC 7099. Other GCs (like NGC 3201 and NGC 6752) show hint of tidal deformation at a low ($\sim 2\sigma$) significance level. Note that, among the 7 GCs with positive detection, in 5 cases (NGC 288, NGC 2298, NGC 5139, NGC 6341, and NGC 7099) the tidal tails extend up to the border of the analysed field of view (at 5° from the

cluster centre) and in two cases (NGC 5139 and NGC 7099) they remain significant at both sides of the cluster covering an extent of $\sim 10^\circ$.

It is also interesting to note that 4 (out of 7) GCs show asymmetric tidal tails. Such an effect is expected in GCs close to their apo/pericentres: in this situation, the velocity of stars varies quickly with the orbital phase so that stars in the leading (trailing) tail move away from the cluster while those in the trailing (leading) tail slowly approach the cluster when it leaves (reaches) the extreme of the orbit. However, while all the 4 GCs exhibiting asymmetric tails are relatively close to their apo/pericentres, in only 2 of them the observed elongation is directed towards the expected direction. So, a more likely explanation is that this evidence is due to statistical fluctuations occurring close to the threshold density which make appear only one side of the tails.

4.2 Comparison with literature works

The GCs analysed in this work have been already studied in the past using different photometric data sets. In particular, the tidal tails of NGC 288 have been discovered up to the same distance from the cluster centre and with the same orientation found in this study by Shipp et al. (2018) using photometric data from the Dark Energy Survey, and Kaderali et al. (2019) using *Gaia* data. Previous studies (Grillmair et al. 1995; Leon et al. 2000; Piatti 2018) also found low-significance distortion close to the tidal radius of this cluster.

Ibata et al. (2019a) used *Gaia* data to detect the same tidal feature observed here around NGC 5139, which appears to be extended for $\sim 28^\circ$ and connected with the previously discovered Fimbulthul stream (Ibata, Malhan & Martin 2019b). The detection of tidal tails around NGC 5139 was also claimed by Leon et al. (2000) but questioned by Law et al. (2003) because of the effect of differential reddening neglected by the former study.

Similarly, Grillmair (2019) found an $\sim 50^\circ$ -extended tidal tails around NGC 5904 using *Gaia* data selected over an area > 6000 sq.deg. Also in this case, small tidal distortions in NGC 5904 were previously reported by Leon et al. (2000) and Jordi & Grebel (2010).

Some density excess close to the tidal radii of NGC 2298 (Leon et al. 2000; Balbinot et al. 2011; Carballo-Bello et al. 2018), NGC 6362 (Kundu et al. 2019) and NGC 7099 (Chun et al. 2010) have been reported in the past. However, none of them reach a comparable level of significance and extent with respect to that found in this work.

No previous studies have found any extratidal feature around NGC 6341.

Among the other GCs analysed here, low-amplitude overdensities outside the tidal radii have been claimed in NGC 1851 (Leon et al. 2000; Carballo-Bello et al. 2018; Shipp et al. 2018), NGC 1904 (Grillmair et al. 1995; Leon et al. 2000; Carballo-Bello et al. 2018; Shipp et al. 2018), NGC 2808 (Grillmair et al. 1995; Chen & Chen 2010; Carballo-Bello et al. 2018), NGC 3201 (Grillmair et al. 1995; Chen & Chen 2010; Bianchini et al. 2019; Kundu, Minniti & Singh 2019), NGC 4590 (Grillmair et al. 1995), NGC 5272 (Leon et al. 2000), NGC 6205 (Leon et al. 2000), NGC 7008 (Grillmair et al. 1995; Chun et al. 2010; Jordi & Grebel 2010), and NGC 7089 (Grillmair et al. 1995). It is not easy to compare the results presented in this paper with those of the above studies, since all of them use different thresholds and smoothing levels and in most cases the identification of extra-tidal features is made on the basis of a qualitative inspection of the density map. Consider also that the lack of detection in this study of significant tidal tails around these GCs could be due to the limiting magnitude of *Gaia* ($20 < G_{\text{cut}} < 21$; see Section 2.2), significantly brighter than those of many of the above studies. This is particularly important in distant GCs where, in spite of the lack of astrometric information, their deep photometry allows to sample the cluster stellar population better by a factor of 10 or more, even in the intrinsically poorly populated periphery of GCs.

4.3 Tidal tails orientation

As introduced in Section 1, because of the different directions of the forces acting on stars within/close to the Jacobi radius and at large distance from the cluster centre, tidal tails are expected to show a characteristic S-shape, with the innermost part elongated towards the Galactic Centre and a torsion towards the cluster orbital path at large distances (Montuori et al. 2007; Klimentowski et al. 2009).

Qualitatively, this prediction seems to be verified in many of the GCs showing extended overdensities outside their tidal radii (see

Figs 2 and 3). In particular, the inner density contours of NGC 288, NGC 5139, NGC 5904, NGC 6362, and NGC 7099 (and with a smaller significance also in NGC 3201 and NGC 6752) appear to be elongated in the direction of the Galactic Centre. On the other hand, in NGC 288, NGC 6341, and NGC 7099, where it is possible to detect the tidal tails up to several degrees, the orientation of the overdensity tends to rotate towards the cluster orbital path.

To quantitatively test the above hypothesis, in the 5 GCs showing the most extended extra-tidal overdensities (NGC 288, NGC 2298, NGC 5139, NGC 6341, and NGC 7099), the field of view outside $0.5 R_J$ has been divided in annuli of 0.1° width and the background-subtracted density of each annulus as a function of the position angle has been fitted with a cosine function. The angle corresponding to the phase of maximum of the best-fitting curve is plotted as a function of the distance from the centre of each of the five considered GCs in Fig. 4. In all cases, the observed orientation is located in the portion of the plane contained between the direction of the orbit and that of the Galactic centre. In NGC 288 and NGC 7099, a drift of the tidal tails position angle from the direction of the Galactic centre to that of the cluster orbit at increasing distances is noticeable.

A χ^2 test applied to regions at $R > R_J$ in each individual GC indicates probabilities 66 per cent $< P_{\chi^2} < 86$ per cent that the distribution of position angles follows the same trend of the orbit.⁵ On the other hand, if all the 5 GCs are considered together, the same test gives a probability of 99.8 per cent, indicating a significant general alignment of the outer portion of the tails with the orbital paths in this sample of GCs.

4.4 Destruction rates

The stars contained in the tidal tails have been lost in recent epochs by the GCs. Although, after its expulsion, the distance of a star from the cluster centre follows a non-monotonic variation with time according to the eccentricity of the cluster orbit (Küpper et al. 2010; Küpper, Lane & Heggie 2012), the phase delay of groups of stars evaporated at different epochs increases with time, so that stars in the tails at increasing distance from the centre were on average expelled at earlier epochs. It is therefore possible to link the fraction of stars contained in the tidal tails with the rate at which a cluster loses its mass through a comparison with suitable models.

For this purpose, as a first step I calculated the number of stars contained in the tidal tails ($N_{\text{obs}}^{\text{tails}}$) and within the cluster tidal radius ($N_{\text{obs}}^{\text{in}}$) in the 5 GCs with the most prominent tidal tails (NGC 288, NGC 2298, NGC 5139, NGC 6341, and NGC 7099). The first quantity has been calculated by integrating the background-subtracted projected density within two 60° -wide regions located at the opposite sides of each cluster at distances $R > 1.5 R_J$ encompassing the tidal tails (see Fig. 5). Unfortunately, the same approach cannot be adopted in the cluster central region characterized by high stellar density and consequently low completeness. So, the number of stars inside the cluster has been estimated by normalizing the projected density profile of the King (1966) model best fit of de Boer et al. (2019) to the density measured in the outer portion of the cluster, which should not be affected by significant crowding. The total number of stars has been then calculated by integrating the model profile from the centre to R_J .

The mass-loss history of each GC has been modelled using the technique of streaklines (Küpper et al. 2012). Briefly, the orbit of

⁵For this test, the averages between the leading and trailing directions of the orbit have been used.

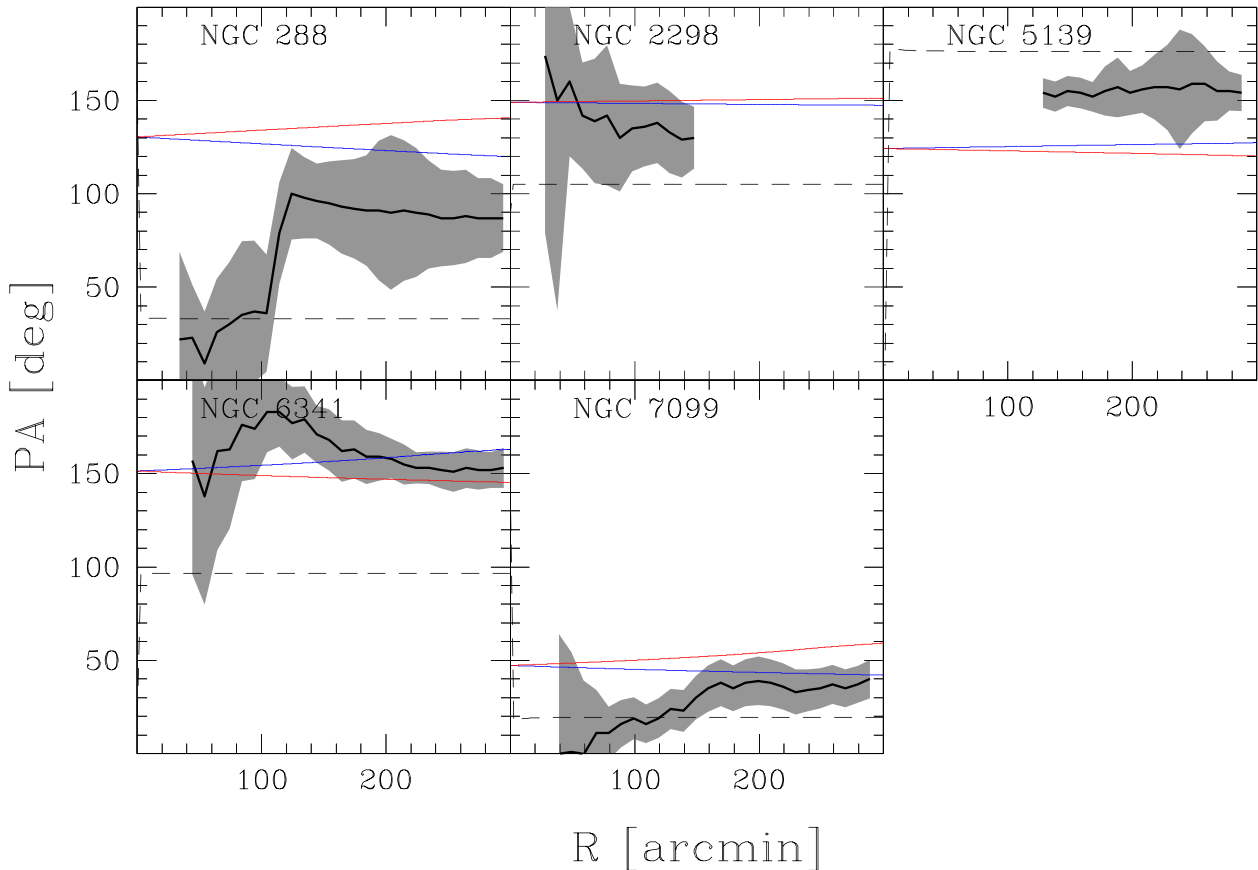


Figure 4. Position angle of the tidal tails as a function of the projected distance from the cluster centre (black solid lines) for NGC 288, NGC 2298, NGC 5139, NGC 6341, and NGC 7099. The shaded area mark the 1σ uncertainty. The direction of the leading (blue lines; dotted lines in the printed version of the paper) and trailing (red lines; dot-dashed lines in the printed version of the paper) sides of the orbit and that to the Galactic Centre (black dashed lines) are overplotted.

each cluster has been reconstructed and, at each integration step, a particle with a small ($\Delta E < 0.1 \text{ km}^2 \text{ s}^{-2}$) positive energy has been put at one of the Lagrangian points and with a velocity directed outward from the cluster. The orbit of each ejected particle and that of the GC (simulated as a point mass particle) have been then followed together within the Galactic potential for 2 Gyr till the present-day position of the cluster. I neglected the cluster mass variation since stars in the portion of the tails analysed here are those ejected at recent epochs in a short time interval (from 0.12 to 1 Gyr depending on the cluster orbit), during which the clusters lost a small (< 6 per cent in all cases) of their present-day mass. This approach is faster than a canonical N -body simulation (since the orbit of the escaped stars are followed individually neglecting mutual interactions and with the relatively long time-step required to accurately integrate their orbit), and has been proven to be effective in reproducing the structure and evolution of tidal tails (Küpper et al. 2012; Mastrobuono-Battisti et al. 2012). As already assumed in Section 4.1, the cluster orbits have been integrated within the Johnston et al. (1995) Galactic potential, using the cluster masses and present-day positions and velocities of Baumgardt et al. (2019). The (constant) mass-loss rate of each simulation has been set to $10^4 \text{ stars Gyr}^{-1}$, which ensures to simulate a statistically significant number of tidal tails stars in a reasonable computation time. At the end of the simulation, the positions and velocities of simulated particles have been converted into equatorial coordinates, proper

motions, and radial velocities. The particles with proper motions within $\Delta\mu < 2 \text{ mas yr}^{-1}$ from the systemic cluster motion and contained within the same regions defined above for observations, have been counted providing the number of predicted stars in tidal tails ($N_{\text{sim}}^{\text{tails}}$) for the assumed mass-loss rate.

The fractions of mass lost per unit time (the so-called ‘destruction rate’) have been therefore calculated as

$$\nu = \frac{10^4 N_{\text{obs}}^{\text{tail}}}{N_{\text{obs}}^{\text{in}} N_{\text{sim}}^{\text{tails}}}$$

and are listed in Table 1.

Of course, many approximations are made in the above estimate: real clusters lose stars non-uniformly during their evolution, and the evolution of the cluster and Galactic potentials are neglected. More importantly, two-body relaxation leads to a preferential loss of low-mass stars, so that the mass function of in the tails is expected to be significantly different from that within the cluster tidal radius (Balbinot & Gieles 2018). So, the estimated mass-loss rates are lower limits to the actual values. In this context, two-body relaxation proceeds in each cluster on different time-scales, so that this effect can affect different clusters in different ways. However, the mass range sampled by *Gaia* is relatively small ($0.6 < M/M_{\odot} < 0.8$) and similar in all the considered GCs, so this effect should affect the above estimate only at a second order.

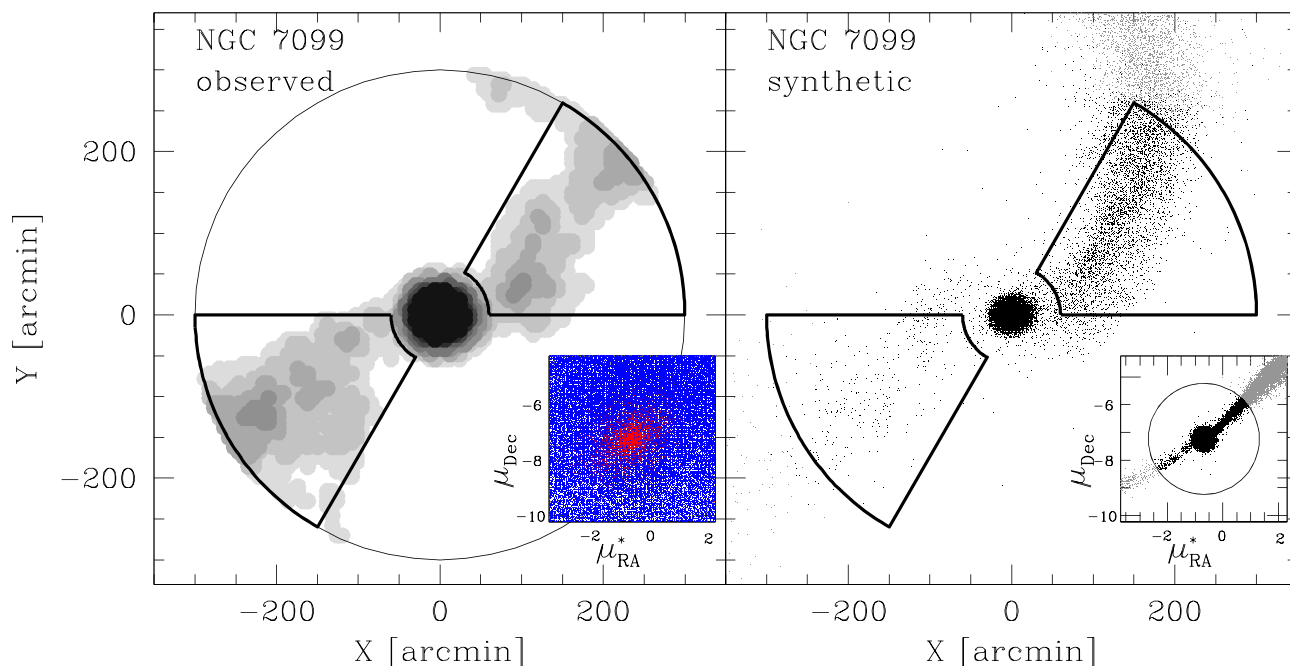


Figure 5. Left-hand panel: observed density map of NGC 7099. The proper motion probability contrast map is plotted in the inset using the same colour code of Fig. 1. Right-hand panel: projected distribution of synthetic particles of the corresponding simulation. The proper motion distribution is shown in the inset. Black and grey dots correspond to particles within and outside the proper motion selection box. The adopted selection boxes are overlotted to both panels as thick black lines.

The derived destruction rates range between $0.018 < \nu/\text{Gyr}^{-1} < 0.085$, corresponding to dissolution times between 12 and 55 Gyr. The destruction rates derived here agree with the predictions calculated for the same GCs of Gnedin & Ostriker (1997) (using Fokker–Planck simulations) and direct N -body simulations (H. Baumgardt; private communication), while they are significantly larger than those reported by Allen et al. (2006). It should be considered that all these theoretical works adopt different Galactic potentials, cluster orbits, and filling factors, so a detailed comparison is not possible.

According to a large number of studies (Gnedin & Ostriker 1997; Balbinot & Gieles 2018) based on theoretical arguments and simulations, the mass-loss rate of a star cluster is determined by the combination of internal (due to two-body relaxation) and external (due to tidal shocks experienced during passages across the Galactic disc and at the peri-Galacticon) effects. The two above processes have different dependences on the cluster characteristics: the internal process is expected to produce an almost constant mass-loss rate every half-mass relaxation time (Spitzer 1987), while the external process depends on the orbital characteristics (Ostriker, Spitzer & Chevalier 1972; Aguilar, Hut & Ostriker 1988). Unfortunately, because of the small number of GCs with significant tidal tails, it is not possible to perform a meaningful analysis of correlations with the parameters affecting the mass-loss. However, at face value, the Pearson correlation coefficients between the logarithm of the destruction rate and those of the half-mass relaxation time (from Baumgardt et al. 2019) and tidal shocks-related destruction rate (given by the sum of equations 1 and 2 of Dinescu et al. 1999) turn out to be -0.60 and 0.36 , respectively. While the small sample size makes both correlations not significant, they are expected since in GCs with short relaxation times two-body relaxation has efficiently

pushed the energy of their stars beyond the escape threshold, and GCs with strong tidal interactions are easily destroyed.

5 CONCLUSIONS

I reported the results of a comprehensive analysis of the projected density map of a sample of 18 Galactic GCs using the set of astrometric and photometric data provided by the *Gaia* second data release. The use of all the available information in the 5D space composed by parallaxes, proper motions, and magnitudes allowed to optimally separate the signal of the cluster population from the contamination from fore/background Galactic field interlopers. This allowed to sample the cluster population down to very faint surface brightness levels.

The derived maps show significant deviation from sphericity close to the tidal radii of many analysed GCs. For 7 (out of 18) GCs these overdensities are statistically significant up to distances exceeding the size of the Roche lobe being likely produced by the strain exerted by the Galactic tidal forces. In 5 GCs the detected overdensities extend up to several degrees from the cluster centre (extending over 10° in NGC 5139 and NGC 7099) and show the typical shape of symmetric tidal tails emerging from the cluster. While for a few GCs (NGC 288, NGC 5139, and NGC 5904) these features were already reported by previous studies (Grillmair et al. 1995; Shipp et al. 2018; Ibata et al. 2019a), the other detections (in NGC 2298, NGC 6341, NGC 6362, and NGC 7099) are new discoveries.

The orientation of the tails follows the predictions of dynamical models: in most of the GCs of the sample, the inner density contours are preferentially aligned with the direction of the Galactic Centre (i.e. the direction of the Galactic potential gradient) which

determines the elongation of the Roche lobe. On the other hand, at large distances the GCs with the most extended features show tidal tails aligned with the orbital path of the cluster. In spite of the uncertainties in the Galactic potential, GC distances, and velocities, this last evidence is statistically significant when the whole set of GCs is considered. In principle, the morphology of the tidal tails could be used to constrain the shape of the Galactic potential (in particular its flattening and the halo-to-disc normalization). However, for this task a larger sample of GCs with tidal tails extending over a wider area than that analysed here would be needed.

For the same set of 5 GCs, the fraction of stars contained in the tidal tails has been used to make the first observational estimate of the present-day mass-loss rate. Till now, these rates have been only predicted simulating the long-term evolution of satellites within a Galactic potential through numerical simulations or analytical prescriptions (Gnedin & Ostriker 1997; Dinescu et al. 1999; Allen et al. 2006). Instead, in this work the destruction rate is directly linked to the observed fraction of stars contained in the visible portion of the tails. Although this estimate is subject to the uncertainties in the amplitude of the low-surface brightness tails and in the normalization of the cluster profile, and neglects many dynamical processes (like e.g. mass segregation; Balbinot & Gieles 2018), it depends only weakly on the modelled orbit and it is linked to an observational feature. Although the small sample size does not allow to draw any firm conclusion, the correlation of the destruction rate with the half-mass relaxation time is stronger than that with the tidal shocks strength, suggesting a dominant role of internal over external dynamical evolution in these GCs. This scenario is in agreement with the evidence of a tight anticorrelation between the mass function slope and half-mass relaxation time observed in a sample of 29 GCs by Sollima & Baumgardt (2017), since dynamically evolved GCs would experience a strong mass-loss which efficiently deplete the low-mass end of their mass functions (Baumgardt & Makino 2003) while producing at the same time prominent tidal tails features. However, further studies based on larger statistical samples are needed to clarify the significance of the above correlations.

The exceptional efficiency of the algorithm presented here is mainly due to the increase of the dimensionality of the available parameter space provided by *Gaia*. Still, the limiting factor is the inhomogeneous sampling at faint magnitudes of this survey which forces the adoption of a cut at relatively bright magnitudes. The next *Gaia* data releases will increase the power of tidal features detection because of the foreseen reduced uncertainties and better spatial sampling.

ACKNOWLEDGEMENTS

I warmly thank Michele Bellazzini for useful discussions and Holger Baumgardt for providing his unpublished destruction rates. I also thank the anonymous referee for his/her helpful comments and suggestions that improved my paper.

REFERENCES

- Aguilar L., Hut P., Ostriker J. P., 1988, *ApJ*, 335, 720
 Allen C., Moreno E., Pichardo B., 2006, *ApJ*, 652, 1150
 Arenou F. et al., 2018, *A&A*, 616, A17
 Balbinot E., Gieles M., 2018, *MNRAS*, 474, 2479
 Balbinot E., Santiago B. X., da Costa L. N., Makler M., Maia M. A. G., 2011, *MNRAS*, 416, 393
 Baumgardt H., Makino J., 2003, *MNRAS*, 340, 227
 Baumgardt H., Hilker M., Sollima A., Bellini A., 2019, *MNRAS*, 482, 5138
 Belokurov V. et al., 2006a, *ApJ*, 642, L137
 Belokurov V., Evans N. W., Irwin M. J., Hewett P. C., Wilkinson M. I., 2006b, *ApJ*, 637, L29
 Bergond G., Leon S., Guibert J., 2001, *A&A*, 377, 462
 Bianchini P., Ibata R., Famaey B., 2019, *ApJ*, 887, L12
 Binney J., Tremaine S., 1987, in Spiegel D. N., ed., *Galactic Dynamics*. Princeton Univ. Press, Princeton NJ
 Bressan A., Marigo P., Girardi L., Salasnich B., Dal Cero C., Rubele S., Nanni A., 2012, *MNRAS*, 427, 127
 Carballo-Bello J. A., 2019, *MNRAS*, 486, 1667
 Carballo-Bello J. A., Martínez-Delgado D., Navarrete C., Catelan M., Muñoz R. R., Antoja T., Sollima A., 2018, *MNRAS*, 474, 683
 Casagrande L., VandenBerg D. A., 2018, *MNRAS*, 479, L102
 Chen C. W., Chen W. P., 2010, *ApJ*, 721, 1790
 Chun S.-H. et al., 2010, *AJ*, 139, 606
 Chun S.-H., Kang M., Jung D., Sohn Y.-J., 2015, *AJ*, 149, 29
 Dalessandro E., Mlocchi P., Carraro G., Jílková L., Moitinho A., 2015, *MNRAS*, 449, 1811
 de Boer T. J. L., Gieles M., Balbinot E., Hénault-Brunet V., Sollima A., Watkins L. L., Claydon I., 2019, *MNRAS*, 485, 4906
 Dinescu D. I., Girard T. M., van Altena W. F., 1999, *AJ*, 117, 1792
 Duc P.-A. et al., 2015, *MNRAS*, 446, 120
 Erkal D., Koposov S. E., Belokurov V., 2017, *MNRAS*, 470, 60
 Fardal M. A., Babul A., Gehean J. J., Guhathakurta P., 2006, *MNRAS*, 366, 1012
 Fukushige T., Heggie D. C., 2000, *MNRAS*, 318, 753
 Gaia Collaboration, 2018a, *A&A*, 616, A1
 Gaia Collaboration, 2018b, *A&A*, 616, A12
 Gnedin O. Y., Ostriker J. P., 1997, *ApJ*, 474, 223
 Goldsbury R., Heyl J., Richer H., 2013, *ApJ*, 778, 57
 Grillmair C. J., 2019, *ApJ*, 884, 174
 Grillmair C. J., Freeman K. C., Irwin M., Quinn P. J., 1995, *AJ*, 109, 2553
 Harris W. E., 1996, *AJ*, 112, 1487
 Ibata R. A., Gilmore G., Irwin M. J., 1994, *Nature*, 370, 194
 Ibata R., Irwin M., Lewis G., Ferguson A. M. N., Tanvir N., 2001, *Nature*, 412, 49
 Ibata R. A., Bellazzini M., Malhan K., Martin N., Bianchini P., 2019a, *Nat. Astron.*, 3, 667
 Ibata R. A., Malhan K., Martin N. F., 2019b, *ApJ*, 872, 152
 Johnston K. V., Spiegel D. N., Hernquist L., 1995, *ApJ*, 451, 598
 Jordi K., Grebel E. K., 2010, *A&A*, 522, A71
 Kaderali S., Hunt J. A. S., Webb J. J., Price-Jones N., Carlberg R., 2019, *MNRAS*, 484, L114
 King I. R., 1966, *AJ*, 71, 64
 Klimentowski J., Łokas E. L., Kazantzidis S., Mayer L., Mamon G. A., Prada F., 2009, *MNRAS*, 400, 2162
 Kundu R., Minniti D., Singh H. P., 2019, *MNRAS*, 483, 1737
 Kundu R., Fernández-Trincado J. G., Minniti D., Singh H. P., Moreno E., Reylé C., Robin A. C., Soto M., 2019, *MNRAS*, 489, 4565
 Küpper A. H. W., Kroupa P., Baumgardt H., Heggie D. C., 2010, *MNRAS*, 401, 105
 Küpper A. H. W., Lane R. R., Heggie D. C., 2012, *MNRAS*, 420, 2700
 Lallement R., Babusiaux C., Vergely J. L., Katz D., Arenou F., Valette B., Hottier C., Capitanio L., 2019, *A&A*, 625, A135
 Law D. R., Majewski S. R., 2010, *ApJ*, 714, 229
 Law D. R., Majewski S. R., Skrutskie M. F., Carpenter J. M., Ayub H. F., 2003, *AJ*, 126, 1871
 Leon S., Meylan G., Combes F., 2000, *A&A*, 359, 907
 Lindgren L. et al., 2018, *A&A*, 616, A2
 Martínez-Delgado D. et al., 2010, *AJ*, 140, 962
 Mastrobuono-Battisti A., Di Matteo P., Montuori M., Haywood M., 2012, *A&A*, 546, L7
 McLachlan G. J., Basford K. E., 1988, in Dekker M., ed., *Statistics: Textbooks and Monographs*. Dekker, New York

- Montuori M., Capuzzo-Dolcetta R., Di Matteo P., Lepinette A., Mocchi P., 2007, *ApJ*, 659, 1212
- Myeong G. C., Jerjen H., Mackey D., Da Costa G. S., 2017, *ApJ*, 840, L25
- Navarrete C., Belokurov V., Koposov S. E., 2017, *ApJ*, 841, L23
- Niederste-Ostholt M., Belokurov V., Evans N. W., Koposov S., Gieles M., Irwin M. J., 2010, *MNRAS*, 408, L66
- Odenkirchen M. et al., 2001, *ApJ*, 548, L165
- Ostriker J. P., Spitzer L., Chevalier R. A., 1972, *ApJ*, 176, L51
- Piatti A. E., 2018, *MNRAS*, 473, 492
- Rockosi C. M. et al., 2002, *AJ*, 124, 349
- Röser S., Schilbach E., 2019, *A&A*, 627, A4
- Röser S., Schilbach E., Goldman B., 2019, *A&A*, 621, L2
- Shipp N. et al., 2018, *ApJ*, 862, 114
- Sollima A., Baumgardt H., 2017, *MNRAS*, 471, 3668
- Sollima A., Martínez-Delgado D., Valls-Gabaud D., Peñarrubia J., 2011, *ApJ*, 726, 47
- Spitzer L., 1987, *Dynamical Evolution of Globular Clusters*. Princeton Univ. Press, Princeton NJ
- Tang S.-Y. et al., 2019, *ApJ*, 877, 12
- Toomre A., Toomre J., 1972, *ApJ*, 178, 623

This paper has been typeset from a $\text{\TeX}/\text{\LaTeX}$ file prepared by the author.